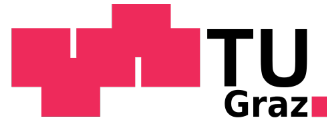

Laurenz Geihofer, BSc

Epitaxial growth and basic material characterization of β-Gallium Oxide

MASTER'S THESIS

to achieve the university degree of

Diplom-Ingenieur

Master's degree programme: Advanced Materials Science

submitted to

Graz University of Technology

Supervisor

Assoc.Prof. Dr. Anna Coclite
Institute for Solid State Physics

Graz, March 2021

The experimental work of this thesis was conducted at

Linköping University

Supervisor

Universitetslektor Dr. Jawad Ul-Hassan
Department of Physics, Chemistry and Biology (IFM)

AFFIDAVIT

I declare that I have authored this thesis independently, that I have not used other than the declared sources/resources, and that I have explicitly indicated all material which has been quoted either literally or by content from the sources used. The text document uploaded to TUGRAZonline is identical to the present master‘s thesis dissertation.

Lorenz Geißhofer

Signature

March 2021

Date

Abstract

Gallium oxide is an up-and-coming ultrawide-bandgap semiconductor. These types of materials have promising properties that could significantly improve the performance of existing applications and enable new technologies. These include high-power electronics, deep-UV optoelectronics and more.

In this work, the heteroepitaxial growth of β-Ga_2O_3, which is the only stable polymorph at standard conditions, through metal-organic chemical vapor deposition is studied. To achieve and optimize film growth, many parameters in the deposition process have to be tuned. In this work, the effect of temperature is investigated. A series of gallium oxide films on c-plane sapphire substrates at a range of different temperatures are grown. These are then analyzed with atomic force microscopy, ellipsometry and X-ray diffractometry to obtain information about surface roughness, thickness, and crystal structure and texture of the grown films.

It could be validated that the grown films consist of mostly epitaxial β-Ga_2O_3, although an amount of a different phase was likely present as well. It was found that changing the growth temperature within the investigated range does not change growth rate, indicating that the deposition at these temperatures happens in the mass transport-limited regime.

Acknowledgements

From Linköping University, I want to thank the following people:

Dr. Jawad Ul-Hassan for supervising my work and always being there to answer my questions, supporting this work in both organizational and scientific matters.

Doctorand Misagh Ghezellou for guiding and helping me tremendously in the laboratory and with the theoretical subject matter.

Professor Vanya Darakchieva for offering me to do this exciting thesis as well as providing financial, organizational and scientific support.

From Graz University of Technology, I want to thank:

Professor Anna Coclite for accepting to be the supervisor from my home university, supporting in organizational and scientific matters despite the distance.

Professor Roland Resel for taking the time to help me with the XRD analyses.

Furthermore, I want to thank my office colleagues and all the other PhD students, post-docs and professors at Linköping University and Graz University of Technology who helped me along the way.

Especially, I want to thank my supervisors for their patience in the challenging times this work was done in, and for their commitment to still enable me to do this thesis the way I was able to.

This work was performed within the competence center for III-Nitride technology, C3Nit — Janzén supported by the Swedish Governmental Agency for Innovation Systems (VINNOVA) under the Competence Center Program Grant No. 2016-05190, Linköping University, Chalmers University of Technology, ABB, Ericsson, Epiluvac, FMV, Gotmic, On Semiconductor, Saab, SweGaN, and UMS. Further support was provided by the Swedish Research Council VR under Award No. 2016-00889 and the Swedish Energy Agency under Award No. P45396-1.

Contents

List of Figures xii

List of Tables xiii

1 Introduction **1**
- 1.1 Material properties of β-Ga_2O_3 1
- 1.2 Potential applications 3
- 1.3 Introduction to bulk growth techniques that have been utilized for β-Ga_2O_3 5
- 1.4 Introduction to other epitaxial growth techniques that have been utilized for β-Ga_2O_3 7
  - 1.4.1 Halide Vapor Phase Epitaxy (HVPE) 7
  - 1.4.2 Mist-Chemical Vapor Deposition (mist-CVD) 7
  - 1.4.3 Molecular Beam Epitaxy (MBE) 8
- 1.5 Introduction to Metal-Organic Chemical Vapor Deposition (MOCVD) 8
  - 1.5.1 Mechanics and setup of MOCVD 8
  - 1.5.2 Chemical reactions in MOCVD 10
  - 1.5.3 Thermodynamics and Kinetics of MOCVD 12
  - 1.5.4 Growth regimes of MOCVD 12
  - 1.5.5 Review of progress in the growth of Ga_2O_3 with MOCVD . 13
- 1.6 Introduction to materials characterization techniques 17
  - 1.6.1 X-Ray Diffractometry (XRD) 17
  - 1.6.2 Atomic Force Microscopy (AFM) 19
  - 1.6.3 Ellipsometry 20

2 Experimental **22**
- 2.1 Substrate preparation 22
- 2.2 Epitaxial growth of β-Ga_2O_3 23
- 2.3 Analytical methods 24
  - 2.3.1 Atomic force microscopy (AFM) 24
  - 2.3.2 Ellipsometry 24

2.3.3 X-Ray diffractometry (XRD) 24

3 Results and discussion **25**

3.1 Overview 25

3.2 AFM 26

3.3 Ellipsometry 28

3.4 XRD 29

3.4.1 2θ-ω measurements 29

3.4.2 Williamson-Hall analysis 32

3.4.3 Pole figure measurements 34

4 Conclusion **37**

Acronyms **39**

Bibliography **40**

List of Figures

1.1 The unit cell of β-Ga_2O_3 2
1.2 Illustration of bulk-growth methods 6
1.3 Simplified schematic of an MOCVD-system 9
1.4 Schematics of bubbler and growth chamber in MOCVD-reactor . . 10
1.5 The reactions in a CVD chamber 11
1.6 The three MOCVD-regimes 13
1.7 Basic schematic of the XRD-setup 17
1.8 X-ray radiation nomencrature 18
1.9 Basic schematic of an atomic force microscope 20
1.10 Illustration of the basic functional principle of ellipsometry 21

3.1 Surface roughness over growth temperature 26
3.2 AFM images 27
3.3 Film thickness over growth temperature 28
3.4 Model of β-Ga_2O_3 unit cell, created with CaRIne 29
3.5 2θ-ω-XRD curves 30
3.6 Relative β-$Ga_2O_3(\bar{2}01)$ intensity and FWHM of XRD peaks 31
3.7 Grain size and microstrains over growth temperature (Williamson-Hall analysis) 33
3.8 Pole figure plots 36

List of Tables

1.1 Comparison of basic properties of β-Ga_2O_3 and other semiconductors 2

1.2 Heteroepitaxy of β-Ga_2O_3: An overview of growth parameters from literature 16

1.3 Homoepitaxy of β-Ga_2O_3: An overview of growth parameters from literature 16

2.1 Sample list 1 (growth parameters overview) 23

3.1 Sample list 2 (analysis results overview) 25

3.2 Calculated and measured angles of peaks in pole figure plots 35

Chapter 1

Introduction

1.1 Material properties of β-Ga_2O_3

Ga_2O_3 exists in five known polymorphs that are named with the greek letters α to ε. Below 1800°C, only the β-phase is stable, though the α-phase is metastable and can also exist under normal conditions [27].

β-Ga_2O_3 has a monoclinic crystal structure and is of the C2/m space group. The lattice parameters are (in Å): a = 12.2, b = 3.0, c = 5.8 [11]. The values for these vary slightly in literature. The unit cell contains 8 gallium atoms in two crystallographically different sites: Ga(I), which is tetrahedrally connected to oxygen atoms, and Ga(II), which has octahedral geometry. The twelve oxygen atoms in three different sites: O(I) and O(II), which both are connected to three gallium atoms, and O(III), which is connected to four gallium atoms [11, 27]. An illustration of the crystal structure can be seen in figure 1.1.

In literature, values for the bandgap of β-Ga_2O_3 vary quite a bit, ranging from about 4.4 to 4.9 eV. The direct bandgap is slightly larger than the indirect bandgap, with the difference reported as a few tens of meV. [11]

The wide bandgap causes a breakdown field that is far larger than that of common semiconductors. It is 8 MV/cm for β-Ga_2O_3.

The thermal conductivity is relatively low compared to other wide- and ultrawide-bandgap semiconductors.

In table 1.1, some basic physical properties of β-Ga_2O_3 are summarized and compared to other wide- and ultrawide-bandgap semiconductors and Silicon.

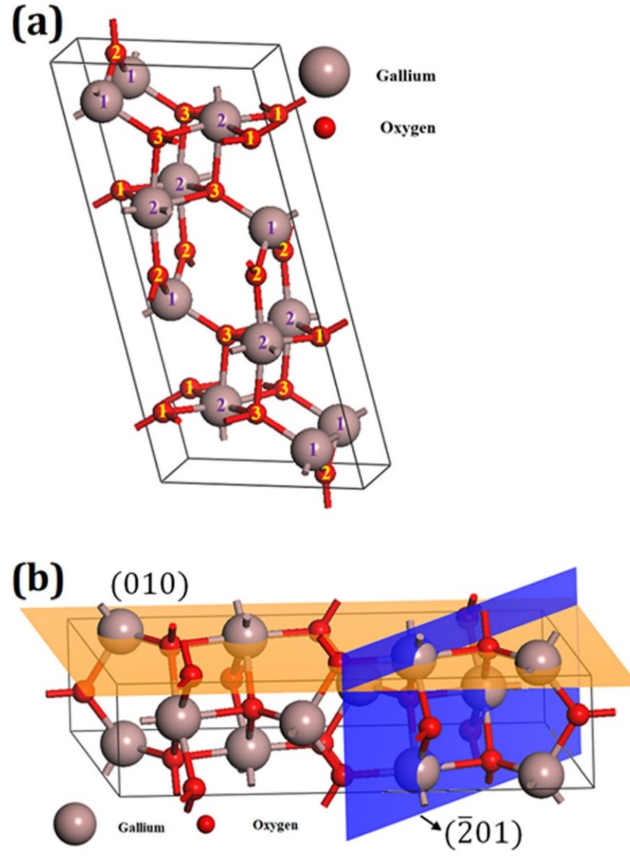

Figure 1.1: (a) The unit cell of β-Ga_2O_3 and (b) (010) and ($\bar{2}01$) surfaces within the crystal structure [27]

Material	Bandgap (eV)		Breakdown field (MV/cm)	BFOM	Thermal Conductivity ($\frac{W}{mK}$)
Si	1.12	indirect	0.3	1	145
GaAs	1.43	direct	0.4	14.7	50
4H-SiC	3.3	indirect	2.5	317	370
GaN	3.4	direct	3.3	846	253
β-Ga_2O_3	4.9	indirect	8	3214	11-27
Diamond	5.5	indirect	10	24 660	2290-3450

Table 1.1: Comparison of basic physical properties and the BFOM of semiconductors with different band gaps. [37, 27]

1.2 Potential applications

Optoelectronics

Solar-blind ultraviolet (UV) detectors are a possible application for which the use of gallium oxide is attractive. Using equations 1.1 and 1.2, one can determine that the cut-off wavelength of β-Ga_2O_3 is at about 250 nm, which is in the deep-UV spectrum of electromagnetic radiation.

$$E = h \cdot f \tag{1.1}$$

$$f \cdot \lambda = c \tag{1.2}$$

Here, E is the energy, h the Planck constant, f the frequency, c the speed of light and λ the wavelength.

Most of the sunlight in the deep-UV region is filtered out by the atmosphere. Because of this, these photodetectors can be sensitive to relatively weak signals even in daylight. [27]

Use in electroluminescent devices is also possible, for example for thin film electroluminescent displays. Doped with rare earth metals, gallium oxide is luminescent at various wavelengths. The chemical and physical stability of gallium oxide could be of advantage. [35]

Power and high-voltage electronics

Perhaps the most exciting use-case for this material are high-power applications. In this field, β-Ga_2O_3 could be used instead of other, narrower-band gap materials that need extensive cooling. For example, schottky diodes using wide-bandgap semiconductors have much higher breakdown fields and much lower R_{on}-values than traditional Si-Schottky diodes, leading to less generated heat. Switching losses have also been shown to be lower in high frequency applications. [27]

Baliga [3] already showed that using wide bandgap semiconductors gives advantages for power applications, doing so by developing a figure of merit. Silicon was compared with large band gap materials; they were considered in the use-case of vertical channel power field effect transistors. To be able to compare them, the fact that the avalanche breakdown voltage is related to the drift region doping level was utilized. Through doping, the compared materials could be tuned to have the same breakdown voltage. It was shown that for vertical channel field effect transistors:

$$R_{ON} \propto \mu^{-1} E_g^{-3} \tag{1.3}$$

where R_{ON} is the on-resistance, μ is the majority carrier mobility and E_g is the band gap of the material. That means that the on-resistance will decrease proportionally

to the majority carrier mobility, and to the third power of the band gap. A figure of merit, known as the Baliga figure of merit (BFOM) was developed [4]:

$$\text{BFOM} = \varepsilon \cdot \mu \cdot E_g^3 \tag{1.4}$$

where ε is the dielectric constant of the material. Sometimes, the critical electric field E_c, where avalanche breakdown happens, is used instead of E_g [27]:

$$\text{BFOM} = \varepsilon \cdot \mu \cdot E_c^3 \tag{1.5}$$

This figure of merit makes comparing the performance of different materials more straight-forward.

Another area in which a higher bandgap is advantageous are high-frequency applications. If a material has a higher breakdown field, it means that the drift region in power MOSFETs can be shortened for the same output voltage, and thus delay times are reduced. The performance advantage of β-Ga_2O_3 in these high-power and high-frequency applications is described in more details in the review articles by [37] and [27]. There, additional figures of merit are discussed and compared to those of other materials.

A potential drawback of β-Ga_2O_3 for the use of power electronics is it's low and anisotropic thermal conductivity of 11 $Wm^{-1}K^{-1}$ in the [100]-direction and 27 $Wm^{-1}K^{-1}$ in the [010]-direction [12]. This might be mitigated by using for example diamond as a heatsink. This and other methods are also being developed for GaN, and could be further developed for gallium oxide [21]. High temperatures want to be avoided in semiconductor materials. Crystal lattice vibrations increase with increasing temperature, and charge carriers can be scattered by them, hindering their mobility. Thus, above a certain temperature, the charge carrier mobility decreases [36, p. 104]. During operation, semiconductor devices can heat up due to Joule heating, and that heat has to be dissipated. The effects of temperature and eventual thermal degradation on performance in β-Ga_2O_3-devices has also been studied and discussed, see for example [8] and [40]. These have shown that thermal considerations will be important in the design of gallium oxide devices.

Gas sensors

Gallium oxide can be used as a sensor for oxygen ($\geq$900 °C) or reducing gases ($<$900 °C). The conductivity of β-Ga_2O_3 is inversely proportional to the partial pressure of oxygen in the environment of the material.

Reported applications are for example the monitoring of exhaust gases, biosensors and ammonia detection. The use of nanocomposites and nanostructured materials can improve the sensitivity of the sensor. [27, 35]

Catalysis

Various catalytic reactions using gallium oxide have been reported, for example catalytic combustion and the oxidation of carbon monoxide. The material can also be used for photocatalysis. UV-light creates electron-hole pairs that can then partake in catalytic reactions. Because the bandgap is higher than in traditionally used materials, the generated electrons have a higher reductive capability. Polymorphism plays an important role in the photocatalytic activity of gallium oxide, but the β-polymorph showed the highest catalytic and photocatalytic activity. Nanostructured materials are interesting for catalysis, as they have a greater surface-to-volume ratio. [35]

1.3 Introduction to bulk growth techniques that have been utilized for β-Ga_2O_3

An advantage of gallium oxide is that native substrates for homoepitaxy are available and can be produced by various melt-growth techniques. An overview over ones that have been used for bulk-growth is given here. Because β-Ga_2O_3 is the most thermally stable form, melt-growth will always result in this polymorph. Pearton et al. [27] gives references to articles that report the use of each of these methods for the growth of gallium oxide.

For the Czochralski method, the material is kept in a crucible at a temperature slightly above its melting point. A seed crystal of the material to be grown is lowered into the melt and then slowly pulled upwards. Single-crystalline material then grows on the seed crystal. The diameter of the grown solid can be increased by lowering the temperature of the melt and vice versa. An illustration of this and the other three mentioned methods can be seen in figure 1.2.

The Float-Zone technique uses a solid rod of poly-crystalline material. A small zone of the rod is melted, and this melted zone is moved from one end to the other. Using a seed crystal on the end of the rod where the melted zone starts, a single crystal can be grown. This method does not use a crucible and leads to highly pure materials. However, due to the heating method, the maximum diameter of crystals is limited.

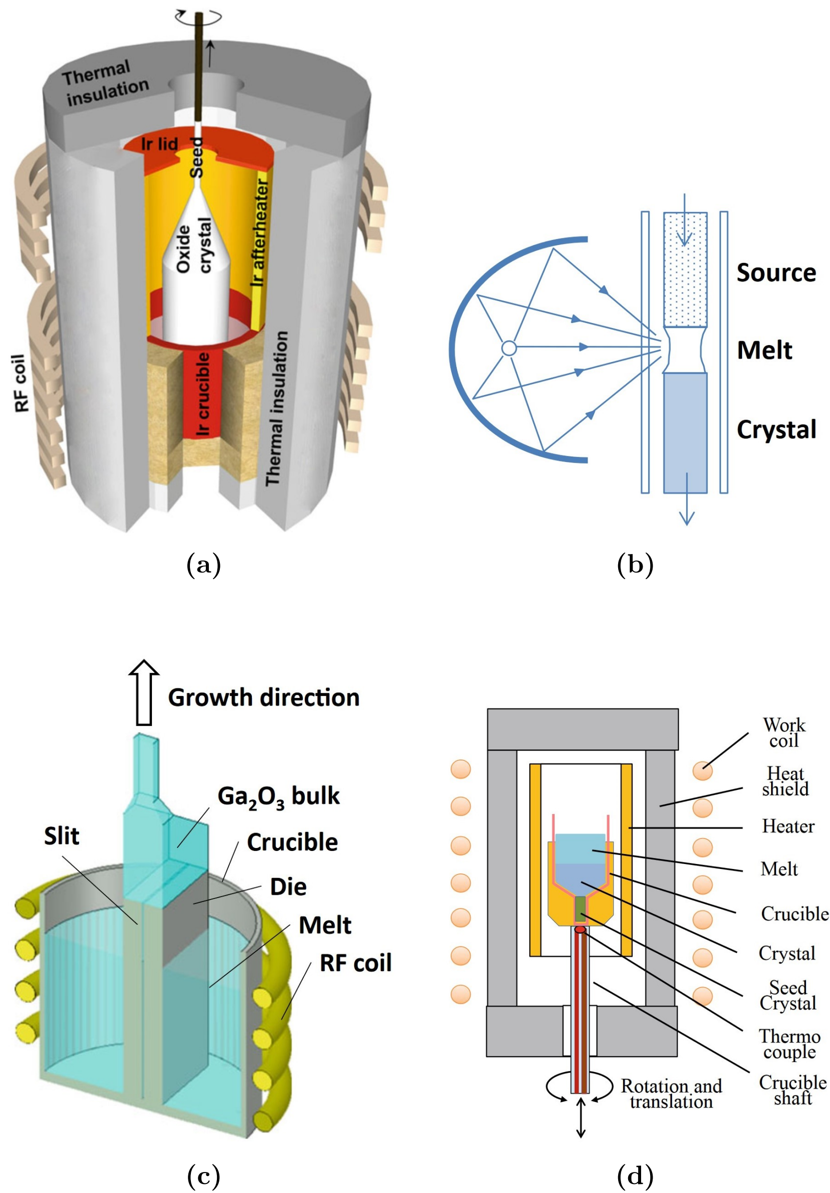

Figure 1.2: Illustrations of the following bulk-growth methods: (a): Czochralski, (b): Floating-zone, (c): Edge-defined film-fed growth, (d): Vertical Bridgman [11]

For the Edge-Defined Film growth method, a die with a capillary hole in the middle is dipped in a crucible filled with a melt of the to-be grown material. The capillary forces pull the melt up the hole. A seed crystal is lowered into the hole and then pulled out. The liquid wets the die, and as the seed crystal is lifted upwards, a single crystal grows in the shape of the die. Thus, differently shaped

crystals can be grown.

In the Bridgman-method, a crucible is kept in a heating chamber above the melting point of the material. It is then moved into a a region with slightly lower temperature, where the melt solidifies. There are horizontal or vertical layouts of this method.

A more detailed look at these techniques is given by [15] and [11].

1.4 Introduction to other epitaxial growth techniques that have been utilized for β-Ga_2O_3

Several growth methods have been tried to grow Gallium Oxide films. In this section, these methods will be introduced. An overview over the outcomes achieved with them will also be given.

1.4.1 Halide Vapor Phase Epitaxy (HVPE)

HVPE is a type of Chemical Vapor deposition (CVD). It achieves high growth rates and high purity for the grown crystals [26]. As the name suggests, halide precursors are used for this method of vapor deposition. As source gases, GaCl was used for Gallium, and O_2 mixed with N_2) was used for Oxygen.

Murakami et al. [23] reported homoepitaxial β-Ga_2O_3-growth on a (001) substrate. At a growth temperature of 1000 °C and a growth rate of 5 µm/h, high purity and high structural quality growth with no twinning was achieved.

Nikolaev et al. [25] used (0001)-sapphire as a substrate. They report epitaxial growth of β-Ga_2O_3 at a temperature of 1050 °C and a growth rate of 70 to 250 µm/h.

Leach et al. [19] reported homoepitaxial growth of β-Ga_2O_3 on a (010)-substrate. Slight miscuts of the substrate toward other directions influenced the morphology of the grown film. On a sapphire substrate, α-Ga_2O_3 was grown. A growth rate of over 25 µm/h was achieved.

1.4.2 Mist-Chemical Vapor Deposition (mist-CVD)

In this method, a solution of the source chemical in water is atomized with ultrasound. The mist produced of the solution in this way is then transported to the reaction chamber with a carrier gas, where the heated substrate is situated [16]. As a substrate, β-Ga_2O_3(010) was used. The reported growth rate at 600 °C was 900 nm/h, and at 900 °C, it was 120 nm/h. At 500 and 600 °C, the grown film was polycrystalline, whereas at 700, 800 & 900 °C, it was almost single crystalline. At

900 °C and above, the surface roughness became worse. Sn-doping was also done by including a Sn-compound in the source solution together with the Ga-source.

1.4.3 Molecular Beam Epitaxy (MBE)

MBE is a physical vapor deposition method. In this ultrahigh vacuum-technique, beams of atoms or molecules are evaporated in elemental effusion cells and deposited on a heated substrate [15].

Sasaki et al. [30] reported successful homoepitaxial β-Ga_2O_3-growth with this method. Pure Ga metal and an Ozone (5%)-Oxygen (95%) mix were used as sources. Here, growth rates of 10 nm/h on the (100)-plane, and of about 125 nm/h on the (010)- and (310)-planes were achieved.

1.5 Introduction to Metal-Organic Chemical Vapor Deposition (MOCVD)

This work focuses on the use of MOCVD for the growth of Gallium Oxide. In the following, an introduction to the method and a review of recent progress in the field is given.

1.5.1 Mechanics and setup of MOCVD

An MOCVD system can be grouped into three parts: The gas delivery system, the growth chamber of the reactor, and the exhaust system. A simplified schematic can bee seen in figure 1.3.

Chemical vapor deposition is a form of vapor thin film deposition in which the precursors undergo chemical reactions to form the final product on the surface of the substrate. MOCVD uses metal-organic precursors, as the name suggests. This precursor is usually in liquid form. In the so-called "bubbler", the bubbler gas is introduced through a tube into the precursor, where it "bubbles" through while taking up vapors from the liquid. The precursors usually have relatively high vapor pressures, which can be modified by changing its temperature. This is done with the use of a precisely controlled temperature bath. The flow rate of the bubbler gas gives another way of controlling the molecular flow rate of the precursor. A schematic of this part is shown in figure 1.4 (a). The gas that comes out of the bubbler is mixed with the carrier gas, which transports it to the growth chamber. For gallium oxide, N_2 or Ar have been used as carrier gases (see section 1.5.5). If doping is wanted, n- or p-type dopant gases can be added through separate bubblers. These usually have to be diluted by mixing outgoing

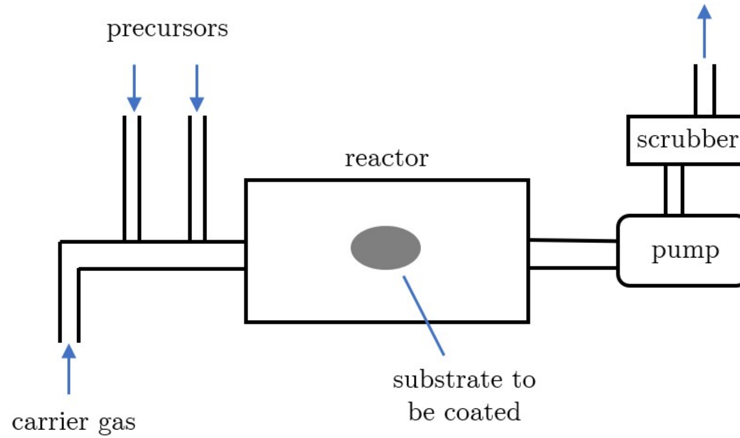

Figure 1.3: Simplified schematic of an MOCVD-system

gas from the bubbler with additional carrier gas. The flow rates and pressures of the various gas lines can be controlled with MFC and pressure controllers.

The growth chamber is where the substrate is positioned. Here, the chemical reactions and the deposition on the surface happen, resulting in the growth of a film on the substrate. The chamber walls are usually made of stainless steel or quartz. Gas flow injector and exhaust are connected to the chamber. Inside, the susceptor is located, on which the substrate is placed. The susceptor is usually made out of graphite and can be heated. In cold-wall reactors, this is the only heat source, which results in a low wall temperature relative to the substrate, hence the name. In the hot-wall reactor used for this work, the growth chamber inside the quartz tube is heated by the means of a radio frequency (RF) coil outside of the tube. To keep the temperature uniformly hot inside this chamber, it is thermally insulated. The substrate can be rotated to obtain a higher growth uniformity. This is done by "gas foil rotation", meaning that a stream of inert gas is used to spin the substrate. There are two main types of reactors that differ by their geometry. In horizontal reactors, the gas flow is parallel to the substrate, and in vertical reactors, it is normal to it. The reactor used in this work is a horizontal, hot-wall MOCVD reactor. A basic schematic of the growth chamber can be seen in figure 1.4 (b).

To keep the pressure inside the growth chamber uniform, the exhaust system has a computer controlled valve. Unreacted molecules or reaction byproducts are transported away to a scrubber, and the cleaned off-gas then exits through the exhaust. For low-pressure reactors, oil-free vacuum pumps are usually used. [14]

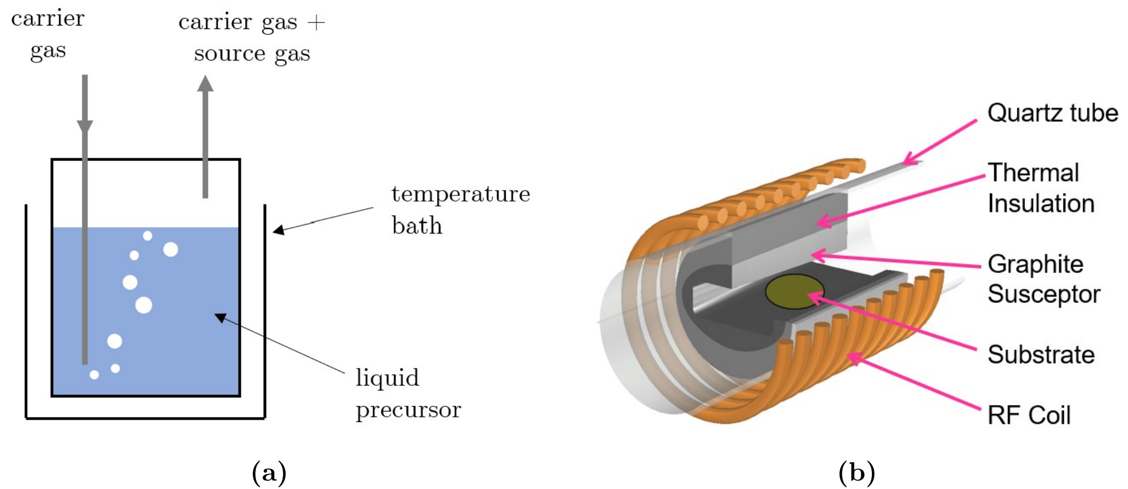

Figure 1.4: Schematics of the following parts of an MOCVD-reactor: (a): Bubbler; (b): Hot-wall MOCVD growth chamber.

1.5.2 Chemical reactions in MOCVD

To show the reaction that is desired to occur, net reaction schemes can be given. These only show the reagents and the products, excluding any intermediate reactions. The net reaction scheme for the growth of gallium oxide with TMGa and O_2 as precursors is given in equation 1.6:

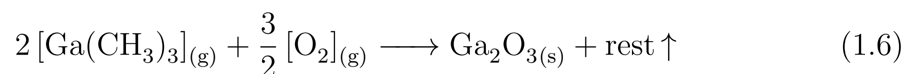

$$2\,[\mathrm{Ga(CH_3)_3}]_{(g)} + \frac{3}{2}\,[\mathrm{O_2}]_{(g)} \longrightarrow \mathrm{Ga_2O_3}_{(s)} + \mathrm{rest}\uparrow \tag{1.6}$$

It is obvious that there have to be some intermediate reactions that take place - the precursors must decompose, so that gallium and oxygen are left over to form the solid state gallium oxide. The general steps that happen are these:

1. Transport of precursors to the growth chamber with a carrier gas;
2. Reactions and pyrolysis of precursors in the gas phase (in hot-wall reactors); these can produce intermediates and by-products;
3. Transport of the reactants through the stagnant region to the surface of the substrate;
4. Adsorption on the surface;
5. Surface diffusion, nucleation, and possible surface chemical reactions, leading to film growth;

6. Desorption and transport of volatile surface reaction products away from the reaction zone and out of the growth chamber.

These steps are also depicted in figure 1.5. Pyrolysis is the thermal decomposition of molecules. This is how the precursors usually decompose in hot-wall CVD. Undesirable, so-called parasitic reactions can also occur in the gas phase. The complete chemical reactions are not fully understood for many materials, but a reaction model has been developed that found over 40 intermediate reactions and by-products for the growth of GaAs from TMGa and AsH_3 [13]. This shows that the processes in MOCVD are very complex.

The stagnant region, also called the boundary layer, is the region above the substrate surface, where gas flow is much slower than in the bulk volume of the reaction chamber.

For TMGa, the pyrolysis can happen homogeneously (purely in the gas phase):

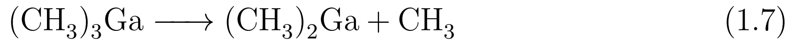

$$(CH_3)_3Ga \longrightarrow (CH_3)_2Ga + CH_3 \tag{1.7}$$

$$(CH_3)_2Ga \longrightarrow (CH_3)Ga + CH_3 \tag{1.8}$$

or heterogeneously (including surface reactions):

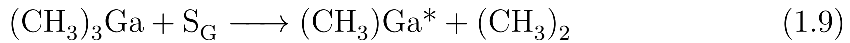

$$(CH_3)_3Ga + S_G \longrightarrow (CH_3)Ga^* + (CH_3)_2 \tag{1.9}$$

for TMGa

$$(CH_3)_2Ga + S_G \longrightarrow (CH_3)Ga^* + CH_3 \tag{1.10}$$

for DMGa. S_G stands for the adsorption site on the surface, and Ga^* indicates the adsorbed species. [14]

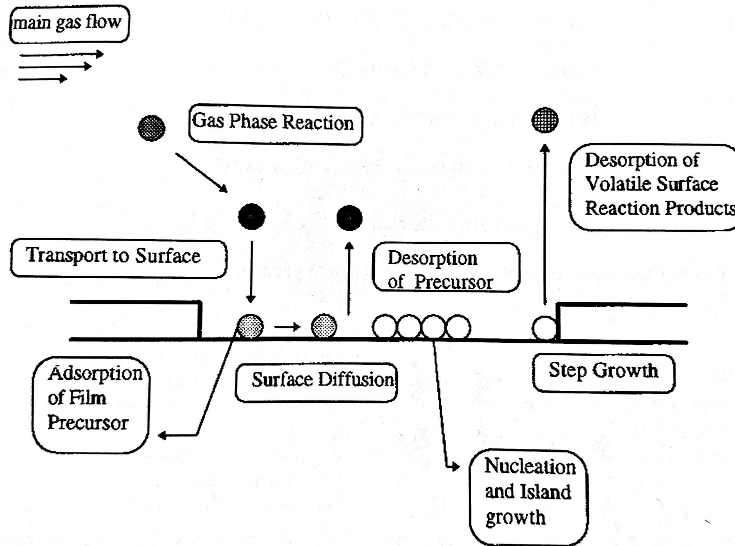

Figure 1.5: The reactions in a CVD chamber [14]

1.5.3 Thermodynamics and Kinetics of MOCVD

Whether a reactions happens or not is determined by thermodynamics and kinetics. The thermodynamics determine if the reaction is energetically favourable. More specifically, this is described by the difference in Gibb's free energy, ΔG, on both sides of the reaction, the so-called driving force.
When the Gibb's free energy G of the gas-phase educts and the solid state product are in equilibrium, no net reaction occurs. In this case that would means no net deposition or desorption. This equilibrium case is given by equation 1.11.

$$2G^{\mathrm{V}}_{\mathrm{Ga}} + 3\, G^{\mathrm{V}}_{\mathrm{O}} = G^{\mathrm{S}}_{\mathrm{Ga_2O_3}} \tag{1.11}$$

Here, V stands for vapour phase, and S stands for solid state.

If however G on one side of the equation is larger than on the other, the system is not in equilibrium, but will try to restore it. When for example the gas phase is supersaturated and has a larger G than the solid state on the substrate surface, there will be a driving force ΔG that will favour deposition. The magnitude of ΔG has an influence on the growth rate.

The Kinetics also have an influence on whether a reaction will happen, and its rate if it does happen. In order for film growth to be possible, the activation free energy ΔG^* must be overcome. This quantity is also related to the growth rate (see equation 1.12).

$$k = \exp(\frac{-\Delta G^*}{RT}) \tag{1.12}$$

Here, k is the rate constant of the reaction, R is the ideal gas constant, and T the temperature. [14]

1.5.4 Growth regimes of MOCVD

The slowest step in the CVD process is the one that limits the growth rate. What the slowest step is depends on growth parameters. Figure 1.6 shows that the rate-limiting step is dependant on temperature. At low temperatures, the surface reactions are limited, and increasing the temperature will increase the growth rate. At intermediate temperatures, the limiting factor is the mass transfer through the stagnant boundary layer. Here, the growth rate is relatively independent of the temperature. At high temperatures, the partial pressure of the precursors near the boundary determines the growth rate, because the vapour pressure on the surface is near the equilibrium. A further increase of temperature can lead to parasitic reactions, deposition on the chamber walls and desorption of adsorbed atoms from the surface as a result of the reversal of the driving force.

Hydrodynamics also play a role in the growth regimes. At pressures > 1 kPa, mass transfer is the controlling factor for growth. At very low pressures (< 1

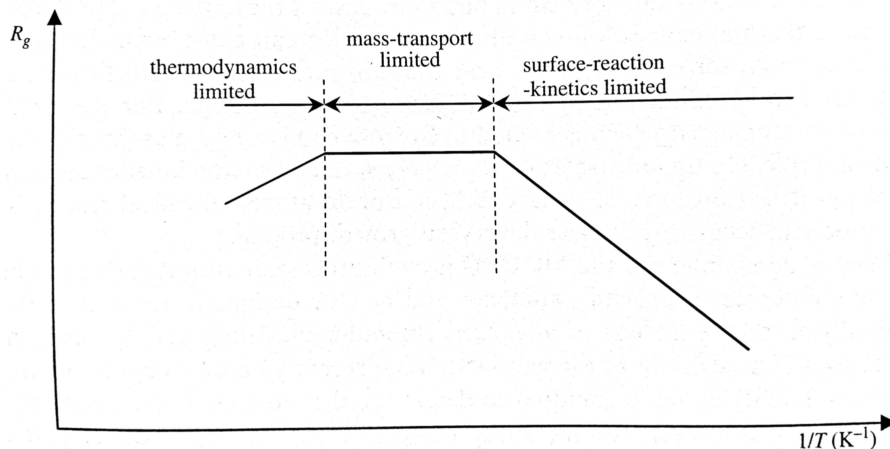

Figure 1.6: The three MOCVD-regimes. Growth rate is depicted as a function of inverse temperature in this diagram. [14]

kPa, called ultralow pressure MOCVD), the growth is only controlled by kinetics, independent of temperature. When even lower pressures (< 10 Pa) are used, it is called ultra-high vacuum-MOCVD. It is employed when precursor molecules should reach the substrate without interacting with other molecules in the gas phase. [14]

1.5.5 Review of progress in the growth of Ga_2O_3 with MOCVD

In the following, a review of literature reporting the hetero- and homoepitaxial growth of gallium oxide is given. This will give an idea about the progress in this field at the time this work was being done. An overview of the growth parameters used in the cited literature is given in tables 1.2 and 1.3. Because not much about the growth of gallium oxide with MOCVD was known at the time this work was done, it was important to collect and summarize the findings of other research groups.

Heteroepitaxy

Gottschalch et al. [10] reported polycrystalline growth on Al_2O_3 and GaAs substrates. Relationships between different sapphire surface planes and epitaxial growth directions of gallium oxide were determined. It was also shown that depending on the sapphire surface plane, only the β, both β and α or only α polymorphs of Ga_2O_3 grow on the substrate. The ratio of α- and β-Ga_2O_3 varied with

temperature. A cold-wall atmospheric pressure reactor was used.

Kim and Kim [18] reported amorphous growth, sometimes containing very small crystallites at the temperatures 500 °C, 550 °C and 600 °C on a Si(100)-substrate. They reported an increasing growth rate with increasing temperature. The surface roughness (RMS) was 0.38, 0.60 and 3.91 nm for the three temperatures, respectively.

Gogova et al. [9] reported β-Ga_2O_3-growth in ($\overline{2}01$)-orientation on Al_2O_3(0001)-substrates. Sn-doped n-type layers were successfully grown. In contrast to the homoepitaxial growth that was also reported (see in the "Homoepitaxy" section), the layers were not single-crystalline.

Mi et al. [22] reported growth at three different temperatures. At 600 °C, the film was amorphous. At 650 °C, the film had a single (100)-orientation, and at 700 °C, a polycrystalline structure was obtained.

Alema et al. [1] also reported epitaxial β-Ga_2O_3-growth in the ($\overline{2}01$)-orientation on Al_2O_3(0001)-substrates.

Schewski et al. [31] reported films with a thickness in a range of 50-150 nm, also in ($\overline{2}01$)-orientation on Al_2O_3(0001)-substrates. Here, three monolayers of α-Ga_2O_3 were grown on the substrate, so that they are between the sapphire and the β-Ga_2O_3.

Cora et al. [6] reported and investigated more closely the structure of so-called ε-Ga_2O_3 on Al_2O_3(0001)-substrates.

Homoepitaxy

Wagner et al. [38] reported that when using O_2 as the oxygen sourece, only nano-wires or -agglomerates could be grown. Using water vapor instead, epitaxial β-Ga_2O_3-growth was achieved, but through transmission electron microscopy (TEM), a high density of twin boundaries and stacking faults was visible. As a substrate, β-Ga_2O_3(100) was used. An increase in temperature resulted in a decrease of the growth rate. The films grown with water vapor showed a surface roughness of 6.5 nm.

Gogova et al. [9] achieved single-crystalline homoepitaxial growth of β-Ga_2O_3 on a (100) substrate with a high assumed density of stacking faults. Sn-doped n-type films were grown. In high resolution-XRD, the (100) peak had a FWHM of 43 arcsec. A surface roughness of 0.4 to 0.6 nm was obtained.

Baldini et al. [2] grew homoepitaxial β-Ga_2O_3 on (010)-substrates. In a TEM image, no crystal defects were seen for the film grown at 850 °C. The surfaces roughness ranged from 0.6 to 11.4 nm, depending on the growth conditions.

Schewski et al. [32] investigated the influence that miscut angles of the (100)-β-Ga_2O_3 substrates have on the structural quality and electronic properties of epitaxially grown layers. It was shown that using identical growth conditions,

differences in miscut angles and directions can change the electron mobility significantly.

Feng et al. [7] reported growth of homoepitaxial, Si-doped layers on (010)-β-Ga_2O_3 substrates. The surface of a representative sample exhibited a roughness of 1.7 nm.

Bin Anooz et al. [5] investigated the growth modes at different growth conditions and different miscut angles. In the case where step-flow growth was achieved, the surface roughness was 0.2 nm. Otherwise, 2D-island growth or step-bunching growth modes occur, and the electron mobility and structural quality is worse. With these growth modes, the surface roughness is higher, with up to 1.5 nm.

number	**reference**	**substrate**	**Ga precursor**	**O precursor**	**carrier gas**	**pressure (mbar)**	**temperature (°C)**	**growth rate (µm/h)**
1	Gottschalch et al. [10]	$Al_2O_3(0001)$, $GaAs(\bar{1}11)$	TEGa	N_2O	N_2	atm.	600-850	0.7
2	Kim and Kim [18]	Si(100)	TMGa	O_2	Ar	-	500-600	~28.2-79.2
4	Gogova et al. [9]	$Al_2O_3(0001)$	TMGa	H_2O	Ar	5-50	775-850	up to 36
6	Mi et al. [22]	$MgAl_6O_{10}(100)$	TMGa	O_2	N_2	high vacuum	600-700	-
7	Alema et al. [1]	$Al_2O_3(0001)$	$Ga(DPM)_3$, TEGa, TMGa	O_2	Ar	40-160	700-950	up to 10
8	Schewski et al. [31]	$Al_2O_3(0001)$	TMGa	H_2O	Ar	5-50	800	-
9	Cora et al. [6]	$Al_2O_3(0001)$	TMGa	H_2O	H_2	-	650	-

Table 1.2: Heteroepitaxy of β-Ga_2O_3: An overview of growth parameters from literature

number	**reference**	**substrate surface orientation**	**Ga precursor**	**O precursor**	**carrier gas**	**pressure (mbar)**	**temperature (°C)**	**growth rate (µm/h)**
3	Wagner et al. [38]	(100)	TMGa	O_2, H_2O	Ar	5-100	750-850	10.8-28.8
4	Gogova et al. [9]	(100)	TMGa	H_2O	Ar	5-50	775-850	up to 36
5	Baldini et al. [2]	(010)	TEGa	O_2	Ar	5	700-850	7.2-19.8
10	Schewski et al. [32]	(100)	TEGa	O_2	Ar	5	825	7.2
11	Feng et al. [7]	(010)	-	-	-	26-133	800-880	-
12	Bin Anooz et al. [5]	(100)	TEGa	O_2	Ar	2-25	825	~5.8-16.5

Table 1.3: Homoepitaxy of β-Ga_2O_3: An overview of growth parameters from literature

1.6 Introduction to materials characterization techniques

1.6.1 X-Ray Diffractometry (XRD)

The distances between atoms in crystal lattices fall in the wavelength spectrum of X-Rays. Thus, X-Rays are a useful tool to examine crystals.

Components

An X-ray source is needed, and in XRD devices, X-ray tubes are used. The working principle of those is as follows: A heated filament acts as a cathode, from which thermoelectrons are accelerated to an anode. Upon hitting the anode X-Rays are generated. They consist of a continuous spectrum of thermal X-Rays and a much stronger set of specific wavelengths that depend on the target anode material. Most commonly used as such is copper. Some of the accelerated electrons eject electrons from the shells of the anode upon hitting it. Figure 1.8 illustrates the nomenclature of these typical X-Rays: If an electron of the K-shell is ejected and another electron from the L shell fills the hole, a photon with the corresponding energy is radiated, and this radiation is called K_α. If the electron comes from the M shell, it is called K_β, and so on. The Cu K_α-radiation has a wavelength of 1.54 Å and is most commonly used. [41, p. 125-127]

After diffraction on the sample, the intensity of the outgoing beam is measured by a detector, allowing to see diffraction maxima and minima. The sample itself is placed on the sample stage, which can be rotated and tilted in some models. The X-ray source, detector and sample can be moved in such ways so as to change the ω and 2θ angles. The X-ray source and detector can be combined with different optical modules. A simplified schematic of the XRD-setup is shown in figure 1.7.

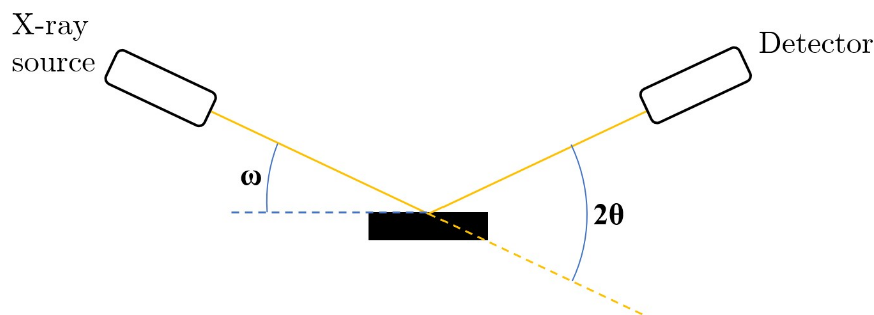

Figure 1.7: Basic schematic of the XRD-setup

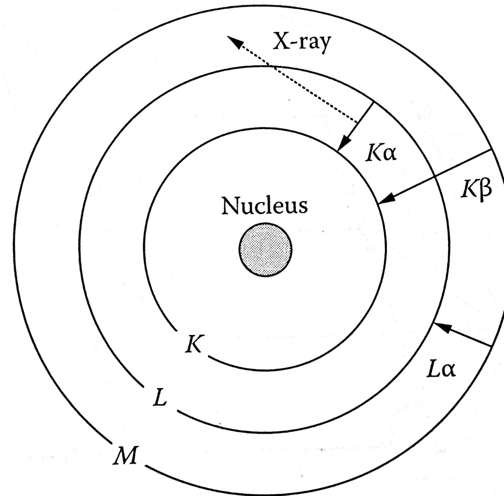

Figure 1.8: The nomenclature of material-specific X-Ray radiation. [41]

Physical principle

The physical principal behind XRD is Bragg's law. The incident X-Ray beam is diffracted upon elastic scattering on the lattice planes of the crystal. Beams diffracted on different lattice planes may interfere with each other destructively or constructively. If they interfere constructively, a maximum is visible on the sensor. Using Bragg's law (equation 1.13), the spacing of the crystal lattice planes can be calculated.

$$2d \sin\theta = n\lambda \tag{1.13}$$

In this equation, d is the lattice spacing, θ is the angle of the X-Ray beam, n is the reflection order and λ is the wavelength. Interference from a greater number diffracted beams of perfect lattice planes results in sharper peaks. Information that can be gained from XRD is crystal structure, crystal size, composition and internal stress.

Operational modes

Different XRD-instruments allow various operational modes, through which this different information is obtained. In the following, the three different modes used in this work are introduced.

Firstly, the X-ray source and the detector can be moved synchronously, so that $\omega = \frac{2\theta}{2}$. This is called a 2θ-ω-measurement, and the obtained curve plots the detected intensity over the 2θ-angle and is used to identify the crystal structure of the sample by checking at which 2θ-angles the peaks occur, and comparing this to

values from a database or a software that can calculate these from crystallographic data.

For the so-called rocking curve measurement, the detector is placed at a 2θ-value of a peak of the sample. The X-ray source is then moved from an angle slightly below θ to slightly above it, resulting in a plot that shows intensity over ω. The full width at half maximum of this peak gives information about the crystalline quality of the sample.

The third operational mode used in this work is the pole figure measurement. For this, both the detector and the sample are fixed at specific $\omega = \frac{2\theta}{2}$ angles of a known peak of the sample. The samples stage then tilts the sample forth and rotates it around an axis perpendicular to the surface, both at specified intervals. The resulting plot shows the intensity at each point on the recorded spherical cap around the axis perpendicular to the surface. With this, the texture of the sample can be studied. Comparing to calculated values, the orientation of specific crystal structures can be obtained.

1.6.2 Atomic Force Microscopy (AFM)

Components

The essential parts of an atomic force microscope are the sample stage, the cantilever with a sharp tip and the detection system. The cantilever commonly consists of silicon and is on the order of 0.1mm long. The tip can be sharp enough for atomic resolution. A simplified schematic of the apparatus is shown in figure 1.9.

Physical principle

The AFM takes topological images by probing the surface of the sample. When the tip gets very close to the surface, it is repelled by atomic forces. This causes the cantilever to bend. The cantilever reflects light from a laser which is then detected by a four-segment photodiode. This way, the bending of the cantilever can be detected.

Operational modes

Different operational modes are available: In contact mode, the tip constantly touches the sample surface. Through a feedback loop, the sample surface can be kept at a constant distance from the tip. How much the sample or the tip have to be moved in order to keep this constant is then mapped, creating the topological image. However, the force exerted on the tip is not only dependent on the distance to the sample surface, but also on other factors like the sample material. Contact

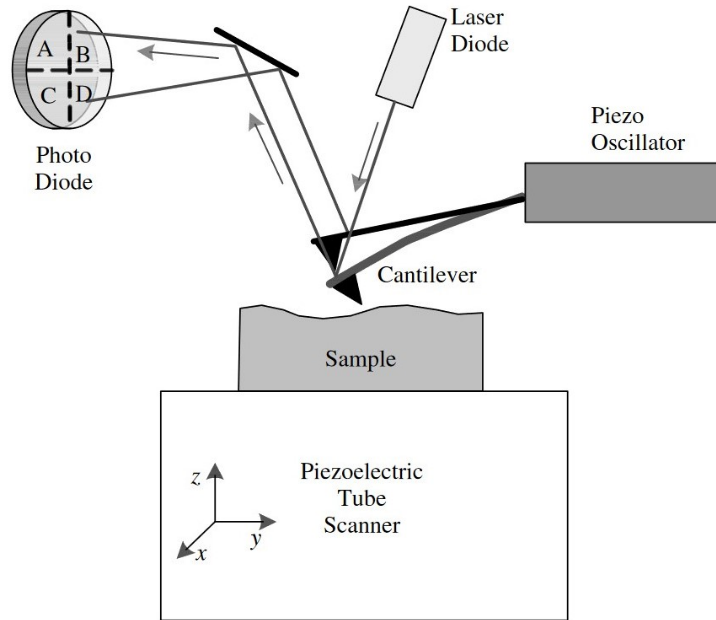

Figure 1.9: Basic schematic of an atomic force microscope. [33]

mode has the disadvantage of potentially damaging the sample surface, so that a repeated scan of the same area could yield different results.

In tapping mode, the cantilever oscillates at a certain frequency while scanning the surface, thus "tapping" instead of dragging over it. The cantilever oscillates close to its resonant frequency. Protruding surface features decrease the oscillation amplitude, depressions in the surface increase it. Here, the amplitude is kept constant through a feedback loop controlling the distance between sample and tip. This way, a topological map is created. Tapping mode mitigates the problem of damaging the sample surface.

Another mode of operation is called non-contact mode. Here, a constant distance between tip and surface is kept, and the Van-der-Waals interaction is measured. This is significantly weaker than the other forces, leading to a lower imaging resolution in this mode. [33]

1.6.3 Ellipsometry

In spectroscopic ellipsometry, unpolarized light passes through polarization filters, creating a beam with a known polarization. The polarization has a component that is parallel to what is called the plane of incidence, referred to as ε_p, and one that is perpendicular to it, reffered to as ε_s. This beam reflects off both the

surface of the film and the interface of film to substrate. Through this reflection and the interference of the reflected beams, the phase and the amplitude of the beam changes. These parameters are detected through comparing the outgoing beam with the incident one. The functioning principle is illustrated in figure 1.10. Ellipsometry is an indirect measurement method, which means that the recorded data does not give the desired quantity to be measured. Instead, models corresponding to certain film thicknesses are created and fitted by a software until they agree with the measured data. [33]

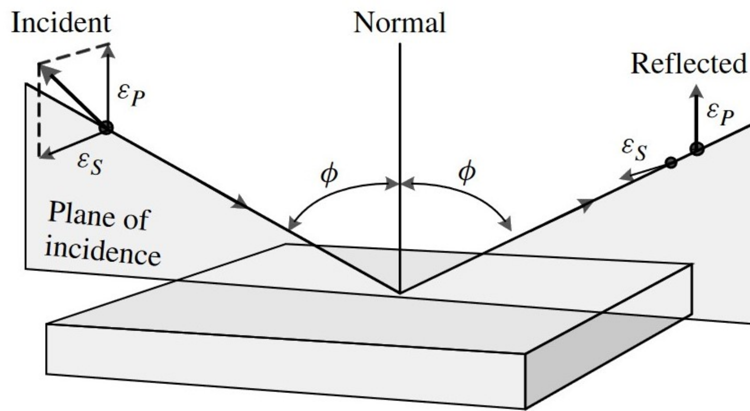

Figure 1.10: Illustration of the basic functional principle of ellipsometry. [33]

Chapter 2

Experimental

The experiments were conducted in the time from June to August 2020 at Linköping University. Because of the Covid-19 situation, this time and the access to the labs was limited. Some analyses could not be repeated in order to get a measure of spread for the results.

2.1 Substrate preparation

The original c-plane sapphire wafers are cut into 1 by 1 cm squares, which are numbered with a diamond pen. Then, they are cleaned with a procedure that was developed by the Radio Corporation of America (RCA) [17]. This is why the main cleaning steps are called "RCA 1" and "RCA 2". In literature, the method is often called RCA cleaning procedure or similar. It was done as follows:

Initial clean This is done to remove fingerprints, heavy residue and organic contamination. The substrates were fully submerged in acetone and put into an ultrasonic bath for 15 minutes. Then, they were rinsed with deionized water.

RCA 1 This is done to remove organic contamination. A solution of 5 parts H_2O, 1 part NH_3 (25 %) and 1 part H_2O_2 (30 %) was prepared; using 125 ml, 25 ml and 25 ml, respectively, in which the substrates were submerged. This was heated up to approximately 85 °C and kept at that temperature for 5 minutes. Afterwards, the substrates were rinsed with water again.

RCA 2 This is done to remove inorganic contamination and particles. The same procedure is done as in RCA 1, but with a solution of 6 parts H_2O, 1 part HCl (37 %) and 1 part H_2O_2 (30 %), using 120 ml, 20 ml and 20 ml, respectively.

Dry After the RCA cleaning process is done, the samples are submerged in ethanol and heated. They are taken out one by one and dried with a N_2-blower and put in the substrate containers.

2.2 Epitaxial growth of β-Ga_2O_3

The thin film was grown in a hot-wall MOCVD reactor. As precursors, TMGa and O_2 were used. As an inert gas, Argon was used. At first, all of the growth parameters were kept at the same values except for the temperature. Seven films were grown, with temperatures of 850, 830, 810, 800, 790, 770 and 750 °C. Analysis of these showed trends indicating better crystalline quality that continued all the way to the lowest growth temperature of 750 °C, so it was decided to do additional growth runs at 700 °C and 650 °C. At this point, analysis showed worse results again, so no further runs at even lower temperatures were done.

It has been shown that an increased ratio of oxygen to gallium-precursor may have a positive impact on crystal growth [5]. This was another area of interest to be investigated. At the time this work was done, it was not possible to increase the oxygen flow rate due to technical limitations. Instead, the TMGa flow was reduced while maintaining the same oxygen flow rate. The last three samples in this list were grown with a slightly lower oxygen flow rate. This was unintentional; the mass flow controllers did not open all the way to the desired value. For the investigation of the effect of lower TMGa- to oxygen-flow ratios, another run (sample 18) was done with the lower oxygen flow rate and the normal TMGa flow rate for comparison. Each growth run was done for two hours.

A list of the samples with information about the growth parameters is given in table 2.1.

Sample name	**Growth temperature (°C)**	**Oxygen flow rate (ml/min)**	Note
11	850	41	
14	830	41	
15	810	41	
13	800	41	
16	790	41	
05	770	41	
06	750	41	
07	700	41	
09	650	34	
18	700	34	
01	700	34	Lower TMGa flow

Table 2.1: Sample list 1 (growth parameters overview)

2.3 Analytical methods

2.3.1 Atomic force microscopy (AFM)

AFM images were taken in tapping mode with horizontal and vertical field widths of 20, 10, 5 and 2 µm, with a resolution of 256 by 256 pixels for each image. The root mean square (RMS) surface roughness was acquired. The instrument used was a Digital Instruments Dimension 3100.

2.3.2 Ellipsometry

Ellipsometry measurements were taken to determine the film thicknesses. The device used was a J.A. Woollam RC2 ellipsometer.

2.3.3 X-Ray diffractometry (XRD)

2θ-ω curves were recorded of all samples. Pole figures were recorded for some samples. The instrument used to obtain the rocking curve and pole figure measurements was the Malvern PANalytical Empyrean system. For the incident beam optics, an X-ray lens was used. As a detector, the PIXcel3D was used together with a parallel plate collimator. For the 2θ-ω measurements, the PANalytical X'Pert PRO system was used.

Chapter 3

Results and discussion

3.1 Overview

Table 3.1 gives a quick look at some analysis results, which will be discussed in detail in the subsequent sections. The "sample name" is simply a number by which the sample has been referred throughout the work and is tied to the substrates.

Sample name	**Growth temperature (°C)**	**FWHM of β-$Ga_2O_3(\bar{2}01)$ rocking curve (°)**	**Film thickness (nm)**	**Surface roughness (RMS), (nm)**
11	850	2.05	125	7.4
14	830	1.77	136	10.0
15	810	1.92	124	9.6
13	800	1.79	124	9.9
16	790	1.67	127	9.9
05	770	1.55	121	7.5
06	750	1.51	125	7.9
07	700	1.43	111	7.3
09	650		123	9.0
18	700		115	5.8
01	700	1.27	92	6.4

Table 3.1: Sample list 2 (analysis results overview)

3.2 AFM

Topological images of 5x5 µm sections the sample surfaces are depicted in figure 3.2. The RMS surface roughness values were taken from 20x20 µm images. They are summarized in table 3.1 and shown as a graph in figure 3.1. The samples grown at temperatures from 790 °C to 830 °C have a rougher surface than the ones grown at lower and higher temperatures. A possible explanation for this is the following: Oxygen is present in the growth chamber before the gallium precursor is introduced. This means that there is a time frame in which the substrate is at the desired temperature but no film growth happens. This might lead to the etching of the substrate surface, changing the morphology of it. A thin film that grows on this surface will be affected by this. At lower temperatures, there might be no or only a low amount of surface etching, leading to a smoother film. At higher temperatures, the substrate might be etched, but in a non-uniform way, leading to a rougher film surface. At even higher temperatures, the etching might become uniform, leading again to a smoother surface.

Sample 01, which was grown with a lower TMGa flow rate, has a slightly lower roughness, but the same is true for the control sample 18. Thus, the lower TMGa flow rate was likely not what caused this difference.

Some reported surface roughness values from literature can be found in section 1.5.5 for comparison.

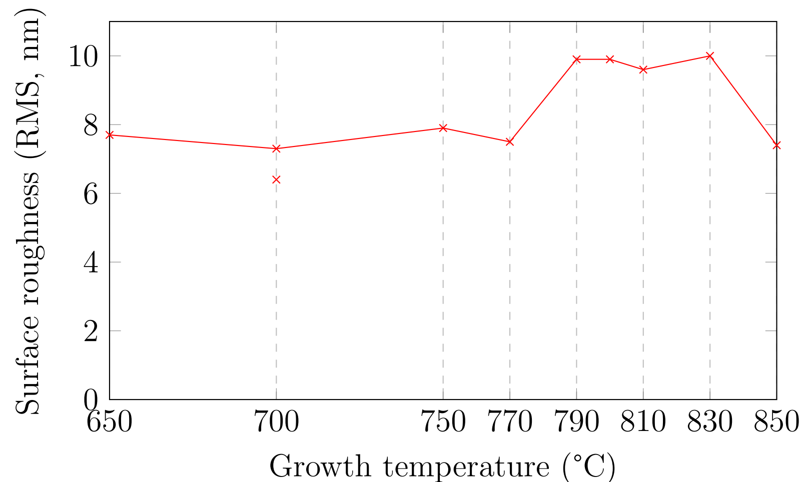

Figure 3.1: Surface roughness (RMS) values of the films grown at different temperatures. Sample 01 which was grown at 700 °C but with lower TMGa-flow is included. It has a lower roughness, but so does sample 18 (not included in this graph, see table 3.1).

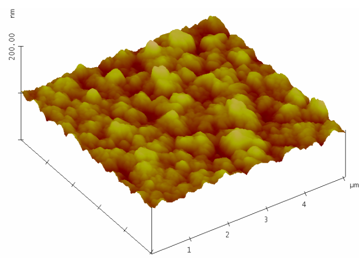

(a) 11 (850 °C)

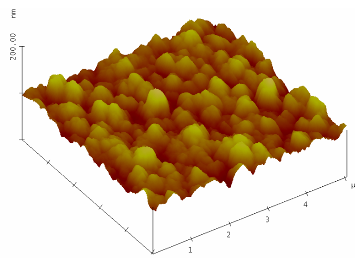

(b) 14 (830 °C)

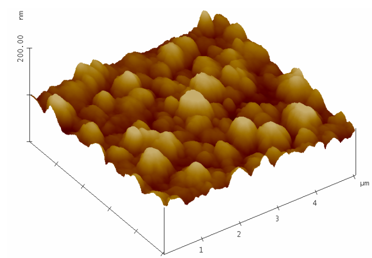

(c) 15 (810 °C)

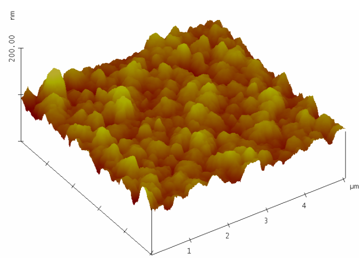

(d) 13 (800 °C)

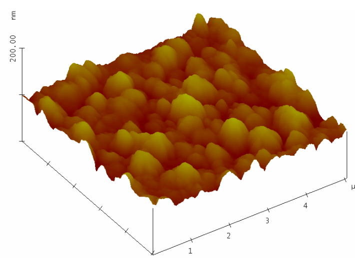

(e) 16 (790 °C)

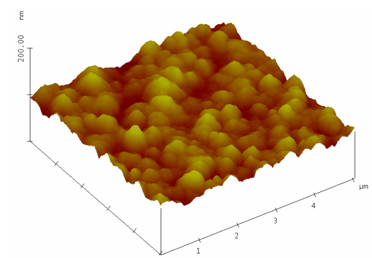

(f) 05 (770 °C)

H

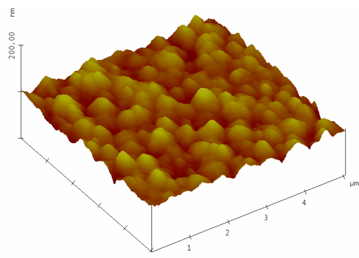

(g) 06 (750 °C)

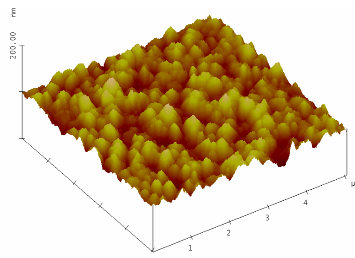

(h) 07 (700 °C)

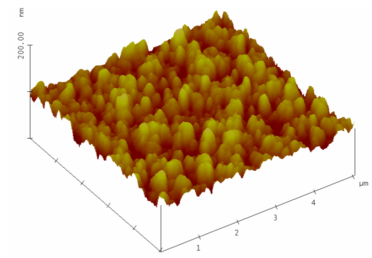

(i) 09 (650 °C)

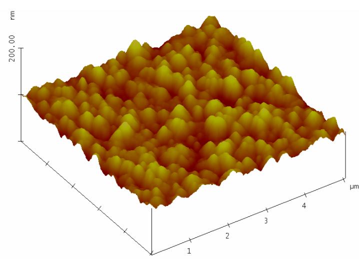

(j) 18 (700 °C)

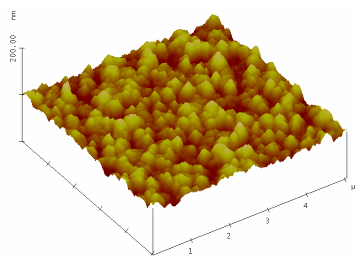

(k) 01 (700 °C, lower TMGa)

Figure 3.2: AFM images of the samples; 5x5 µm, y-axis: ±200 nm.

3.3 Ellipsometry

The thicknesses of the films were measured with ellipsometry. As seen in figure 3.3, the thickness stays at a similar value throughout the temperature series. This means that the deposition in the MOCVD-reactor happens in the mass-transport limited regime (see section 1.5.4) throughout the entire temperature range used. What supports this further is the fact that sample 01, which was grown at 700 °C, but with a lower TMGa flow rate, is thinner than sample 18, which is grown with the higher TMGa flow rate but otherwise the same parameters.

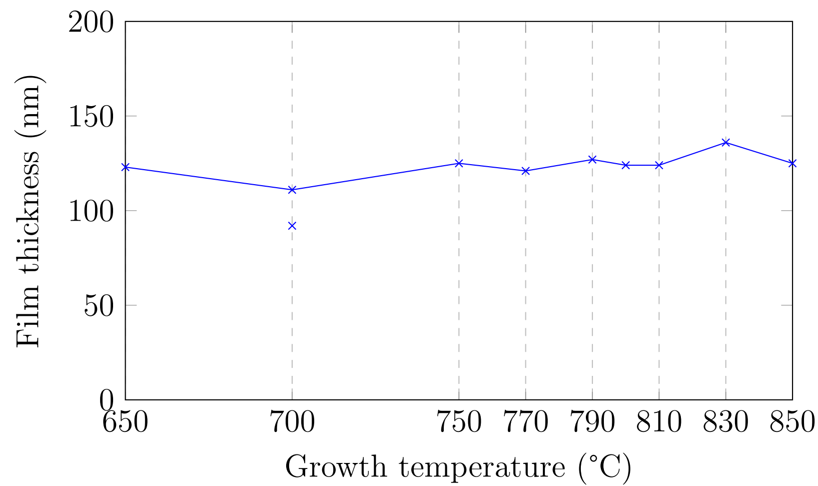

Figure 3.3: Film thickness values for the films grown at different temperatures. Sample 01, which was grown at 700 °C but with lower TMGa-flow has a lower thickness.

3.4 XRD

3.4.1 2θ-ω measurements

2θ-ω XRD-curves were recorded for all samples. Here, the $(\bar{2}01)$, $(\bar{4}02)$ and $(\bar{6}03)$ peaks can be seen (see figure 3.5). The values for the 2θ-angles corresponding to these crystal planes calculated with the software CaRIne are 18.93 °, 38.40 ° and 59.12 °. Because it is a family of planes, these three angles are spaced at approximately the same interval. The experimentally determined values correspond well to these calculated values. Since these are by far the most prominent peaks in these data - excepting the sapphire peak from the substrate - it can be assumed that the films consist of mostly β-Ga_2O_3 with $(\bar{2}01)$-orientation. This is investigated further with pole figure measurements (see section 3.4.3).

CaRIne is a software that allows the modelling of crystal structures. Powder diffraction XRD peaks can be calculated, as well as peaks expected in pole figure measurements. The values for the positions of the atoms within the unit cell are taken from [29]. A model of the β-Ga_2O_3 unit cell created with CaRIne is depicted in figure 3.4.

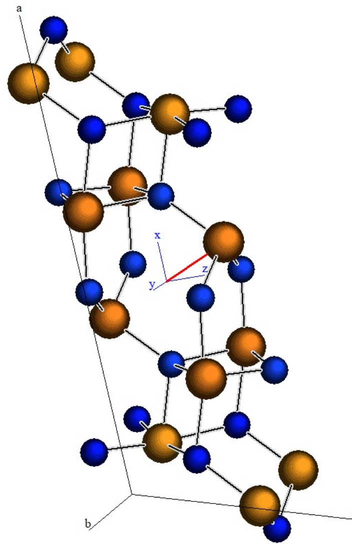

Figure 3.4: Model of β-Ga_2O_3 unit cell, created with the software CaRIne.

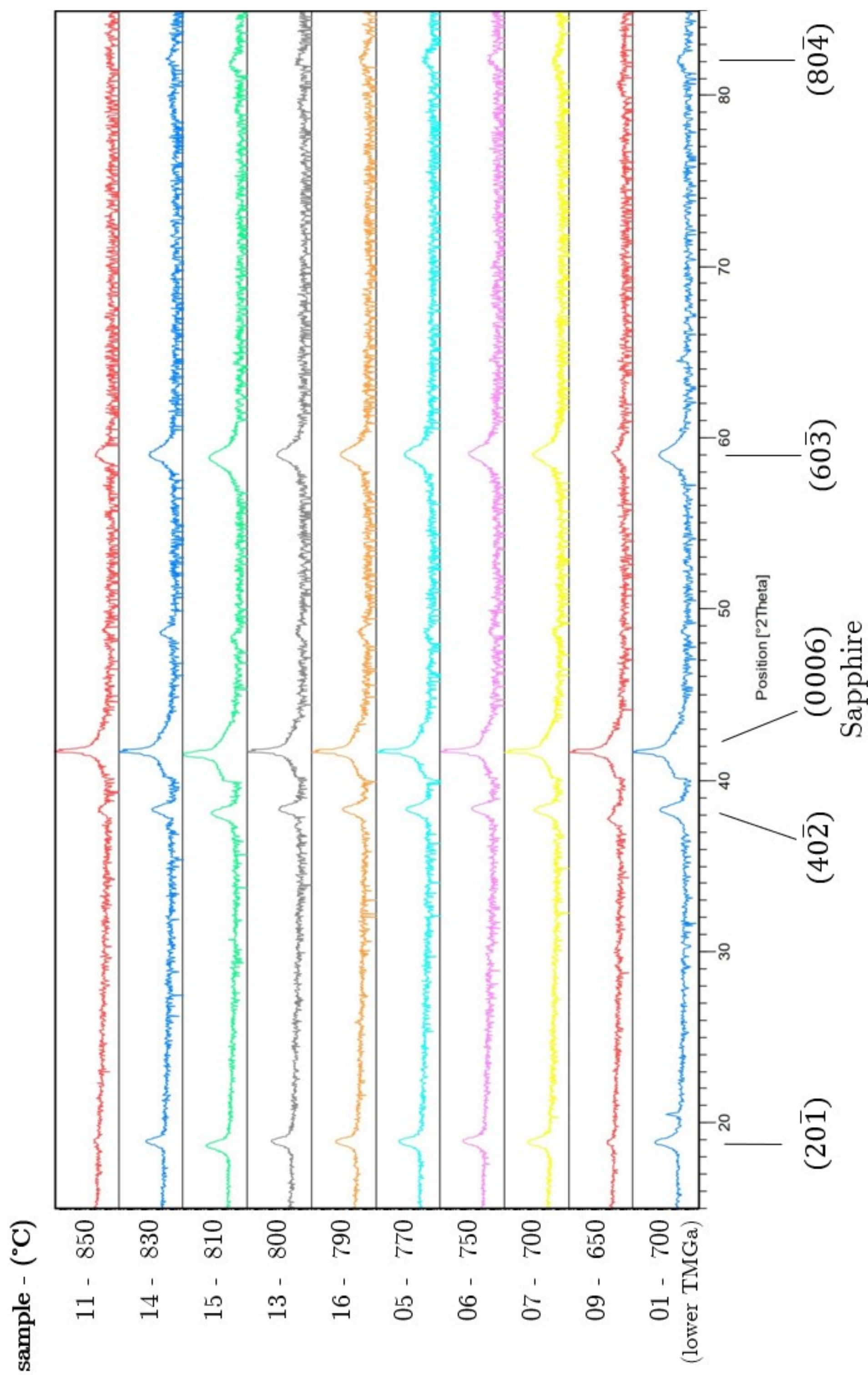

Figure 3.5: Comparison of the 2θ-ω-XRD curves.

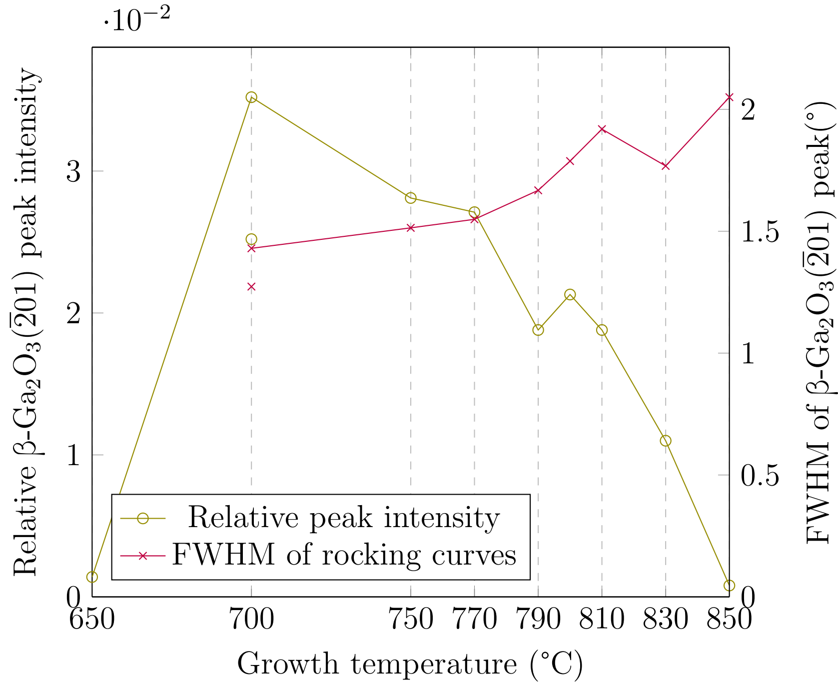

Figure 3.6: The relative β-$Ga_2O_3(\bar{2}01)$ peak intensity to the sapphire (0006) peak as well as the FWHM acquired in rocking curve measurements of the $(\bar{2}01)$ peak are shown here. The lower values for both of the graphs are the ones for sample 01, which was grown with a lower TMGa flow rate.

For the 2θ-ω XRD curves that were recorded, the ratio of the maximum intensity of the sapphire (0006) peak and the β-Ga_2O_3 $(\bar{2}01)$ peak were calculated. When this ratio is plotted in a graph (see figure 3.6), a trend can be seen: The intensity of the $(\bar{2}01)$-peak of β-Ga_2O_3 is increasing (in relation to the sapphire (0006)-peak) with decreasing growth temperature, until this trend is reversed completely at 650 °C. The film grown with a lower TMGa flow rate has a lower peak intensity, which could be due to its lower thickness.

Rocking curve measurements were also done for the $(\bar{2}01)$-peaks of the samples and show a similar trend. The FWHM of the peaks generally decreases from 850 °C all the way down to 700 °C (see figure 3.6). The value for the film grown at 650 °C is not included in the plot, because for that sample, the peaks was too undefined to determine a FWHM. The film grown at 700 °C with a lower TMGa flow rate has a narrower peak. In literature, an FWHM of this peak for β-Ga_2O_3 thin films grown on c-plane sapphire by different methods have been reported at around 1 ° [20, 28].

Because of these trends, it is assumed that a temperature of around 700°C gives the best conditions for the growth of β-Ga_2O_3 thin films with the other parameters

set to the values used in this work.

All samples show a low peak at about 48.5 °, but it is most pronounced in sample 14 (see figure 3.5). This peak most likely stems from a different crystal structure. β-Ga_2O_3 does have peaks at about this 2θ-angle, namely the (510)- and (003)-peaks at 2θ=48.59 ° and 48.42 °, respectively. However, if it were β-Ga_2O_3-crystallites with one of those two orientations parallel to the surface that caused this peak, then these grains should cause additional peaks in the pole figures. For example, the $(\bar{2}01)$-peak of those crystallites should be visible at about $\chi = 62$ ° in the pole figures recorded at $2\theta = 18.9$ °. However, no such peaks are visible (see figure 3.8).

An effect that has not been studied here, which could however have an influence on the growth, quality and structure of the films is the possible inclusion of impurities. A source for carbon impurities could stem for example from the susceptor, which is made out of graphite.

3.4.2 Williamson-Hall analysis

Two factors contribute to the broadening of peaks in XRD: Grain size - smaller grains lead to stronger broadening - and microstrains. An analysis method has been developed that allows the investigation of both of those factors with the use of the 2θ-ω curves [39].

For this analysis, one needs more than one peak, ideally multiple from a family of planes; i.e., h,k,l and higher order peaks nh,nk,nl. In this case, we use the $(\bar{2}01)$, $(\bar{4}02)$ and $(\bar{6}03)$-peaks of β-Ga_2O_3, which are clearly visible in the data.

The effect of crystallite size on peak broadening is given in equation 3.1:

$$\Delta(2\theta) = \frac{\lambda}{D\cos\theta} \tag{3.1}$$

Where $\Delta(2\theta)$ is the FWHM of the peak, λ the wavelength of the X-rays and D the crystallite size.

The effect of microstrains or defects, which cause variations in interplanar distances, is given in equation 3.2:

$$\Delta(2\theta) = 2\frac{\Delta a}{a}\tan\theta \tag{3.2}$$

Where a is the lattice constant and $\frac{\Delta a}{a}$ a measure for microstrains.

We can then add these two components and rearrange to achieve a linear equation in the form $y = kx + d$:

$$\Delta(2\theta)\cos\theta = 2\frac{\Delta a}{a}\sin\theta + \frac{\lambda}{D} \tag{3.3}$$

The part on the left side of the equation is now our y of the linear equation, and $\sin\theta$ corresponds to x. We can then take the FWHM- and θ-values of our three peaks and use them to calculate three points that are expected to be on a linear slope. A linear fit can then be applied. From the intercept of this fit with the y-axis, the grain size can be deduced. The incline of the fit gives a measure for the microstrains.

Figure 3.7 shows the grain sizes and microstrains for the films grown at various temperatures as calculated with this method.

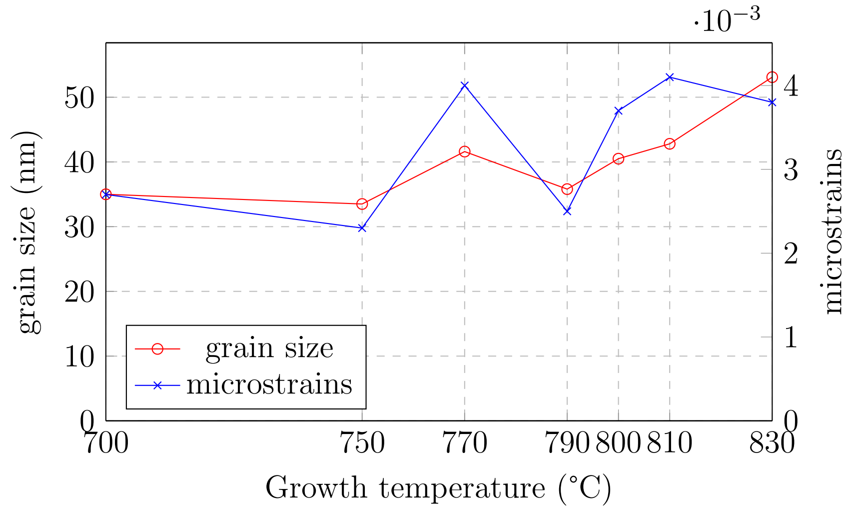

Figure 3.7: Grain size and microstrains of the thin films at various temperatures, as calculated with the Williamsen-Hall analysis.

The peaks in the 2θ-ω-curves of the samples grown at 650 °C and 850 °C were not defined enough to do this analyis. The margin of error of this method is quite high, meaning that this method does not give a very accurate picture of the crystallite sizes in the film. A general idea of the size of the grains is given nonetheless, which is that they are about a third to a half of the film thickness. Furthermore, a trend can be seen, showing slightly larger grain sizes at the higher growth temperatures. This could be caused the higher mobility of adsorbed atoms from the gas phase during growth. For the microstrains, a slight trend towards higher strains at higher growth temperature can be seen.

3.4.3 Pole figure measurements

To investigate the crystal structure and texture of the thin films, pole figure measurements were done on the following four samples: 11 (850 °C), 06 (750 °C), 07 (700 °C) and 01 (700 °C, lower TMGa flow). Table 3.2 gives an overview of the expected and measured angles for the pole figures, and the angles where peaks were recorded. The positions of the peaks on the plots were the same for all four samples. Comparing the recorded peaks to the the calculated values for the different crystal orientations and polymorphs of gallium oxide, one can see that the only clear peaks visible are ones corresponding to $(\overline{2}01)$-β-Ga_2O_3.

Very noticable for all peaks not at $\chi = 0$ ° is their six-fold symmetry. All of them are visible six times at their respective χ-values at intervals of $\varphi = 60$ °, rotated around the center in the pole figures. From this, it can be deducted that the thin film is not single crystalline. The crystal grains in the thin film responsible for these peaks, while all having their $(\overline{2}01)$-planes parallel to the surface, are rotated at intervals of 60 ° around an axis perpendicular to the surface. Because for every six-fold, the peaks are at similar strength, it can be assumed that the rotational distribution of the grains is even. Seiler et al. [34] and Nakagomi and Kokubun [24] explain the epitaxial relationship between c-plane sapphire and β-Ga_2O_3, including how this six-fold symmetry comes to be.

Additionally, there were some unexpected peaks for sample 11 in the pole figure done at $2\theta = 31.7$ ° that occur at $\chi = 80$ ° and also exhibit a six-fold symmetry (see (c) in figure 3.8). These cannot be caused by $(\overline{2}01)$-β-Ga_2O_3 grains, as there are no crystal planes with a spacing that would lead to peaks close enough to $2\theta = 31.7$ ° at a surface tilt of about 80 °. The same is true for (0001)-Al_2O_3. The origin of these peaks could not be determined in the frame of this work.

2θ (°) calc.	**2θ (°) meas.**	**χ (°) experim.**	**χ (°) β-Ga_2O_3 calculated**			**χ (°) α-Ga_2O_3 calculated**	
			(hkl)	**texture ($\bar{2}$01)**	**texture (101)**	**(hkl)**	**texture (002)**
18.93	18.9	0	($\bar{2}$01)	0	72.39	(002)	0
30.05 30.45	30	25, 55	(400) ($\bar{4}$01)	53.89 23.50	53.72 84.11	(013)	0
31.73 31.76	31.7	22.5, 50	($\bar{2}$02) (002)	22.52 49.97	49.86 22.45	(031) (122)	72.71 54.67

Table 3.2: The first column gives the calculated 2θ-values where peaks are expected in the pole figures. The second column are the angles at which measurements were done. Column 3 gives the angles at which peaks were recorded. The further columns gives the corresponding χ-values where peaks are expected - the values for β-Ga_2O_3 were calculated with CaRIne, the α-Ga_2O_3 values are taken from [34].

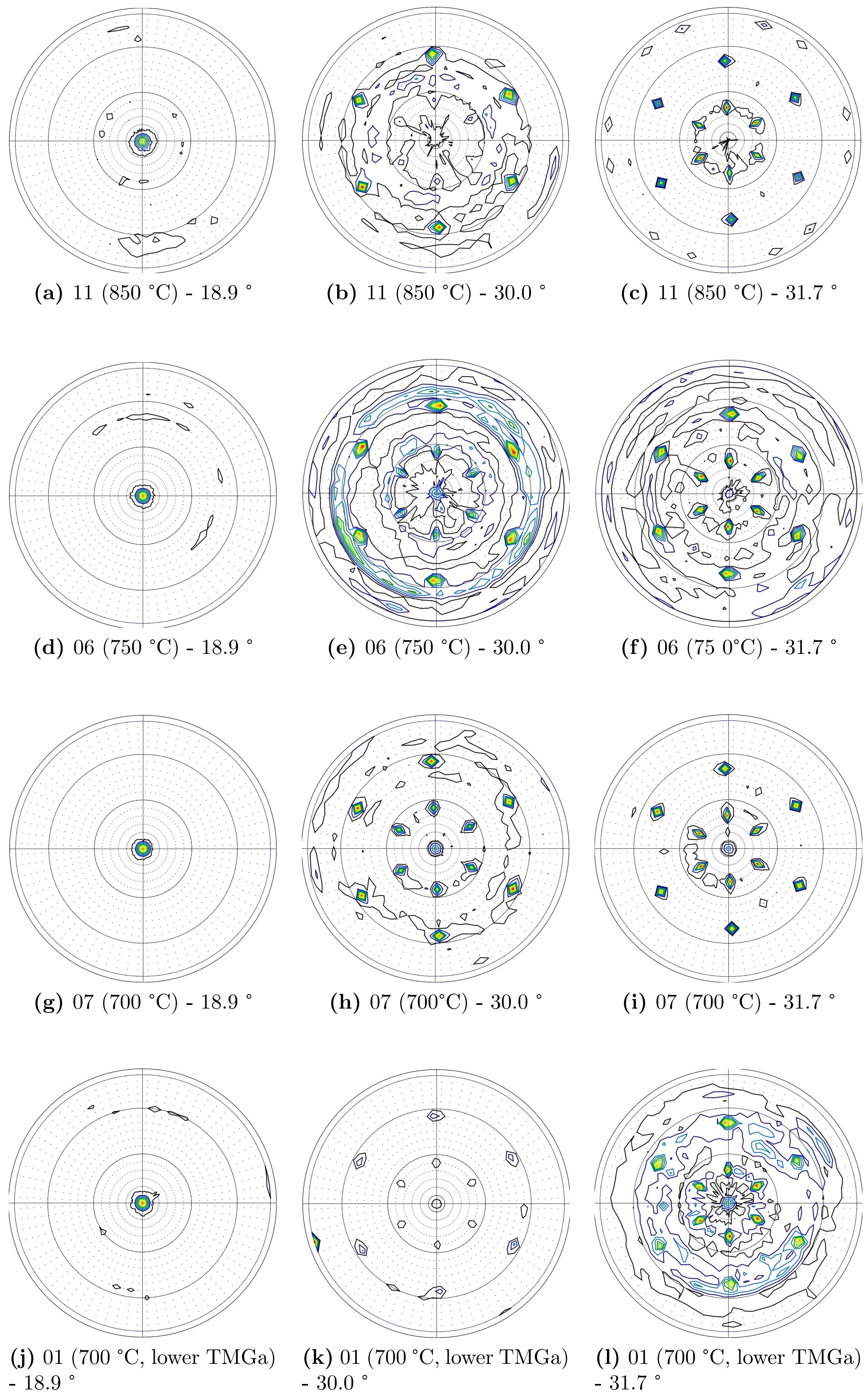

(a) 11 (850 °C) - 18.9 °
(b) 11 (850 °C) - 30.0 °
(c) 11 (850 °C) - 31.7 °

(d) 06 (750 °C) - 18.9 °
(e) 06 (750 °C) - 30.0 °
(f) 06 (75 0°C) - 31.7 °

(g) 07 (700 °C) - 18.9 °
(h) 07 (700°C) - 30.0 °
(i) 07 (700 °C) - 31.7 °

(j) 01 (700 °C, lower TMGa) - 18.9 °
(k) 01 (700 °C, lower TMGa) - 30.0 °
(l) 01 (700 °C, lower TMGa) - 31.7 °

Figure 3.8: Pole figure plots (sample name, growth temperature, 2θ-value)

Chapter 4

Conclusion

The goal of this work was to achieve heteroepitaxial growth of β-Ga_2O_3 thin films. Since the growth of gallium oxide through MOCVD is relatively new and unexplored, the effect of different growth parameters on film growth with a new reactor has to be investigated. The main goal of work was to study the effect of growth temperature. Furthermore, the effect of a different TMGa to oxygen flow rate ratio was explored.

Films were grown on c-plane sapphire substrates in a horizontal hot-wall MOCVD reactor in a temperature range from 850 °C to 650 °C. The samples were then analysed with AFM, ellipsometry and XRD. With the help of the AFM, an idea about the surface roughness of the films was given: From 830 °C to 790 °C, the roughness was slightly above that of the films grown at higher and lower temperatures. A possible explanation for this could be the non-uniform etching of the substrate surface at a certain temperature range, before the gallium precursor is introduced to the chamber.

The thicknesses of the films was around 120 nm after a deposition of two hours, meaning that the growth rate is about 60 nm per hour. No trend correlating to growth temperature was found. Decreasing the TMGa flow rate led to a decrease of growth rate. Both of those factors indicate that at the investigated temperature range, the vapour deposition is in the mass-transport limited regime. The growth rate compared to literature values (see section 1.5.5) is relatively slow.

With the help of XRD, 2θ-ω, rocking curve and pole figure measurements were taken. This gave information about the crystal structure and texture. It was shown that β-Ga_2O_3 crystallites with the $(\bar{2}01)$-plane parallel to the substrate surface were grown. They are rotated in a six-fold symmetry around an axis perpendicular to the surface. Possibly, an amount of crystallites of another structure were included in the film, of which the origin could not be determined. It is possible that they are of a different gallium oxide polymorph. The β-Ga_2O_3 peaks were strongest relative to the substrate peak at a growth temperature of 700 °C. Similarly, the FWHM

of the rocking curves were smallest at this growth temperature. This suggests that 700 °C is most suited for the growth of β-Ga_2O_3 thin films in this reactor. A Williamsen-Hall analysis was done, which showed that the grain size in the thin films is about a third to a half of the thickness of the films.

The growth of β-Ga_2O_3 thin films was a success, and a good idea about the effects of temperature was given, laying a groundwork for further research and development of the MOCVD of this up-and-coming ultrawide-bandgap semiconductor material. One of the next steps in that process is for example to study the effect of a significantly increased oxygen flow, which could not be done in this work due to technical limitations of the reactor at that time. This is assumed to significantly increase the growth rate, as indicated in literature [5]. Furthermore, the homoepitaxial growth on native β-Ga_2O_3 substrates can be investigated.

Acronyms

AFM atomic force microscopy. x–xii, 19, 24, 26, 27, 37

BFOM Baliga's figure of merit. 2, 4

FWHM full width at half maximum. xii, 14, 25, 31–33, 37

HVPE halide vapor phase epitaxy. x, 7

MBE molecular beam epitaxy. x, 8

MFC mass flow controller. 9

MOCVD metal-organic chemical vapor deposition. x, xii, 8–13, 23, 28, 37, 38

MOSFET metal-oxide field-effect transistor. 4

RCA Radio Corporation of America. 22, 23

RF radio frequency. 9

UV ultraviolet. 3, 5

XRD X-ray diffractometry. x–xii, 14, 17, 18, 24, 29–32, 37

Bibliography

[1] F. Alema, B. Hertog, A. Osinsky, P. Mukhopadhyay, M. Toporkov, and W. V. Schoenfeld. Fast growth rate of epitaxial β–ga2o3 by close coupled showerhead mocvd. *Journal of Crystal Growth*, 475:77–82, 2017.

[2] M. Baldini, M. Albrecht, A. Fiedler, K. Irmscher, R. Schewski, and G. Wagner. Si-and sn-doped homoepitaxial β-ga2o3 layers grown by movpe on (010)-oriented substrates. *ECS Journal of Solid State Science and Technology*, 6 (2):Q3040, 2016.

[3] B. J. Baliga. Semiconductors for high-voltage, vertical channel field-effect transistors. *Journal of applied Physics*, 53(3):1759–1764, 1982.

[4] B. J. Baliga. Power semiconductor device figure of merit for high-frequency applications. *IEEE Electron Device Letters*, 10(10):455–457, 1989.

[5] S. Bin Anooz, R. Grüneberg, C. Wouters, R. Schewski, M. Albrecht, A. Fiedler, K. Irmscher, Z. Galazka, W. Miller, G. Wagner, et al. Step flow growth of β-ga2o3 thin films on vicinal (100) β-ga2o3 substrates grown by movpe. *Applied Physics Letters*, 116(18):182106, 2020.

[6] I. Cora, F. Mezzadri, F. Boschi, M. Bosi, M. Čaplovičová, G. Calestani, I. Dódony, B. Pécz, and R. Fornari. The real structure of ε-ga 2 o 3 and its relation to κ-phase. *CrystEngComm*, 19(11):1509–1516, 2017.

[7] Z. Feng, A. Anhar Uddin Bhuiyan, M. R. Karim, and H. Zhao. Mocvd homoepitaxy of si-doped (010) β-ga2o3 thin films with superior transport properties. *Applied Physics Letters*, 114(25):250601, 2019.

[8] M. Fujii, Y. Uraoka, T. Fuyuki, J. S. Jung, and J. Y. Kwon. Experimental and theoretical analysis of degradation in ga2o3–in2o3–zno thin-film transistors. *Japanese Journal of Applied Physics*, 48(4S):04C091, 2009.

[9] D. Gogova, M. Schmidbauer, and A. Kwasniewski. Homo-and heteroepitaxial growth of sn-doped β-ga 2 o 3 layers by movpe. *CrystEngComm*, 17(35): 6744–6752, 2015.

[10] V. Gottschalch, K. Mergenthaler, G. Wagner, J. Bauer, H. Paetzelt, C. Sturm, and U. Teschner. Growth of β-ga2o3 on al2o3 and gaas using metal-organic vapor-phase epitaxy. *physica status solidi (a)*, 206(2):243–249, 2009.

[11] M. Higashiwaki and S. Fujita. *Gallium Oxide: Materials Properties, Crystal Growth, and Devices*, volume 293. Springer Nature, 2020.

[12] M. Higashiwaki, K. Sasaki, H. Murakami, Y. Kumagai, A. Koukitu, A. Kuramata, T. Masui, and S. Yamakoshi. Recent progress in ga2o3 power devices. *Semiconductor Science and Technology*, 31(3):034001, 2016.

[13] K. F. Jensen, D. I. Fotiadis, and T. J. Mountziaris. Detailed models of the movpe process. *Journal of crystal growth*, 107(1-4):1–11, 1991.

[14] A. C. Jones and M. L. Hitchman. *Chemical vapour deposition: precursors, processes and applications.* Royal society of chemistry, 2009.

[15] S. Kasap and P. Capper. *Springer handbook of electronic and photonic materials.* Springer, 2017.

[16] T. Kawaharamura, H. Nishinaka, and S. Fujita. Growth of crystalline zinc oxide thin films by fine-channel-mist chemical vapor deposition. *Japanese Journal of Applied Physics*, 47(6R):4669, 2008.

[17] W. Kern. Cleaning solution based on hydrogen peroxide for use in silicon semiconductor technology. *RCA review*, 31:187–205, 1970.

[18] H. W. Kim and N. H. Kim. Growth of gallium oxide thin films on silicon by the metal organic chemical vapor deposition method. *Materials Science and Engineering: B*, 110(1):34–37, 2004.

[19] J. Leach, K. Udwary, J. Rumsey, G. Dodson, H. Splawn, and K. Evans. Halide vapor phase epitaxial growth of β-ga2o3 and α-ga2o3 films. *APL Materials*, 7(2):022504, 2019.

[20] X. Liu, P. Guo, T. Sheng, L. Qian, W. Zhang, and Y. Li. β-ga2o3 thin films on sapphire pre-seeded by homo-self-templated buffer layer for solar-blind uv photodetector. *Optical Materials*, 51:203–207, 2016.

[21] M. A. Mastro, A. Kuramata, J. Calkins, J. Kim, F. Ren, and S. Pearton. Perspective—opportunities and future directions for ga2o3. *ECS Journal of Solid State Science and Technology*, 6(5):P356, 2017.

[22] W. Mi, C. Luan, Z. Li, C. Zhao, X. Feng, and J. Ma. Ultraviolet–green photoluminescence of β-ga2o3 films deposited on mgal6o10 (1 0 0) substrate. *Optical Materials*, 35(12):2624–2628, 2013.

[23] H. Murakami, K. Nomura, K. Goto, K. Sasaki, K. Kawara, Q. T. Thieu, R. Togashi, Y. Kumagai, M. Higashiwaki, A. Kuramata, et al. Homoepitaxial growth of β-ga2o3 layers by halide vapor phase epitaxy. *Applied Physics Express*, 8(1):015503, 2014.

[24] S. Nakagomi and Y. Kokubun. Crystal orientation of β-ga2o3 thin films formed on c-plane and a-plane sapphire substrate. *Journal of crystal growth*, 349(1):12–18, 2012.

[25] V. Nikolaev, A. Pechnikov, S. Stepanov, I. Nikitina, A. Smirnov, A. Chikiryaka, S. Sharofidinov, V. Bougrov, and A. Romanov. Epitaxial growth of (2 01) β-ga2o3 on (0001) sapphire substrates by halide vapour phase epitaxy. *Materials Science in Semiconductor Processing*, 47:16–19, 2016.

[26] Y. Oshima, E. G. Víllora, and K. Shimamura. Halide vapor phase epitaxy of twin-free α-ga2o3 on sapphire (0001) substrates. *Applied Physics Express*, 8 (5):055501, 2015.

[27] S. Pearton, J. Yang, P. H. Cary IV, F. Ren, J. Kim, M. J. Tadjer, and M. A. Mastro. A review of ga2o3 materials, processing, and devices. *Applied Physics Reviews*, 5(1):011301, 2018.

[28] S. Rafique, L. Han, A. T. Neal, S. Mou, M. J. Tadjer, R. H. French, and H. Zhao. Heteroepitaxy of n-type β-ga2o3 thin films on sapphire substrate by low pressure chemical vapor deposition. *Applied Physics Letters*, 109(13): 132103, 2016.

[29] D. Roehrens, J. Brendt, D. Samuelis, and M. Martin. On the ammonolysis of ga2o3: An xrd, neutron diffraction and xas investigation of the oxygen-rich part of the system ga2o3–gan. *Journal of Solid State Chemistry*, 183(3): 532–541, 2010.

[30] K. Sasaki, A. Kuramata, T. Masui, E. G. Villora, K. Shimamura, and S. Yamakoshi. Device-quality β-ga2o3 epitaxial films fabricated by ozone molecular beam epitaxy. *Applied Physics Express*, 5(3):035502, 2012.

[31] R. Schewski, G. Wagner, M. Baldini, D. Gogova, Z. Galazka, T. Schulz, T. Remmele, T. Markurt, H. von Wenckstern, M. Grundmann, et al. Epitaxial stabilization of pseudomorphic α-ga2o3 on sapphire (0001). *Applied Physics Express*, 8(1):011101, 2014.

[32] R. Schewski, K. Lion, A. Fiedler, C. Wouters, A. Popp, S. V. Levchenko, T. Schulz, M. Schmidbauer, S. Bin Anooz, R. Grüneberg, et al. Step-flow growth in homoepitaxy of β-ga2o3 (100)—the influence of the miscut direction and faceting. *APL Materials*, 7(2):022515, 2019.

[33] D. K. Schroder. *Semiconductor material and device characterization*. John Wiley & Sons, 2015.

[34] W. Seiler, M. Selmane, K. Abdelouhadi, and J. Perrière. Epitaxial growth of gallium oxide films on c-cut sapphire substrate. *Thin Solid Films*, 589: 556–562, 2015.

[35] S. Stepanov, V. Nikolaev, V. Bougrov, and A. Romanov. Gallium oxide: Properties and applica 498 a review. *Rev. Adv. Mater. Sci*, 44:63–86, 2016.

[36] B. G. Streetman, S. Banerjee, et al. *Solid state electronic devices*. Prentice Hall, 2005.

[37] J. Tsao, S. Chowdhury, M. Hollis, D. Jena, N. Johnson, K. Jones, R. Kaplar, S. Rajan, C. Van de Walle, E. Bellotti, et al. Ultrawide-bandgap semiconductors: Research opportunities and challenges. *Advanced Electronic Materials*, 4(1):1600501, 2018.

[38] G. Wagner, M. Baldini, D. Gogova, M. Schmidbauer, R. Schewski, M. Albrecht, Z. Galazka, D. Klimm, and R. Fornari. Homoepitaxial growth of β-ga2o3 layers by metal-organic vapor phase epitaxy. *physica status solidi (a)*, 211(1):27–33, 2014.

[39] G. Williamson and W. Hall. X-ray line broadening from filed aluminium and wolfram. *Acta metallurgica*, 1(1):22–31, 1953.

[40] M. H. Wong, Y. Morikawa, K. Sasaki, A. Kuramata, S. Yamakoshi, and M. Higashiwaki. Characterization of channel temperature in ga2o3 metal-oxide-semiconductor field-effect transistors by electrical measurements and thermal modeling. *Applied Physics Letters*, 109(19):193503, 2016.

[41] S. Zhang, L. Li, and A. Kumar. *Materials characterization techniques*. CRC press, 2008.